Supporting Information for

"Freezing" Intermediate Phase for Efficient and Stable $FAPbI_3$ Perovskite Solar Cells

Muyang Chen,[1] Tingting Niu,[1] Lingfeng Chao,[1] Xiaozheng Duan,[2] Jingpei Wang,[1] Tengfei Pan,[1] Yajing Li,[1] Junhan Zhang,[3] Chenyue Wang,[3] Biyun Ren,[1] Lijuan Guo,[1] Mohammad Hatamvand,[1] Jing Zhang,[4] Qingxun Guo,[1] Yingdong Xia,[1] Xingyu Gao,[3] Yonghua Chen[1*]

*Corresponding author. Email: iamyhchen@njtech.edu.cn (Y.C.)

Methods

Materials

DMF (Sigma-Aldrich, anhydrous, 99.8%); DMSO (Sigma-Aldrich, anhydrous, 99.9%); Isopropanol (IPA) (Sigma-Aldrich, anhydrous, 99.9%); Diethyl ether (Yonghua Chemical Co., Ltd, China, anhydrous, 99.7%); Dehydrated ethanol (Sigma-Aldrich, anhydrous, 99%); Formamidinium iodide (FAI, GreatCell Solar, 99.9%); Methylammonium chloride (MACl, GreatCell Solar, 99.9%); Lead iodide (PbI_2, Advanced Election Technology Co., Ltd, China, 99.99%); SnO_2 (Alfa Aesar, 15% in H_2O colloidal dispersion); Chlorobenzene (CB, Sigma-Aldrich, 99.99%); n-Octylammonium iodide (OAI, Sigma-Aldrich, 99.99%); Spiro-OMeTAD (Advanced Election Technology Co., Ltd, China); Acetonitrile (ACN) (Sigma-Aldrich, 99.9%); Lithiumbis(trifluoromethyl sulfonyl)imide (Li-TFSI; 99.95%, Sigma-Aldrich); 4-tertbutylpyri-dine (tBP, 99.9%, Sigma-Aldrich).

Preparation of the Precursor

For all precursor solutions, 1.7 M PbI_2, 1.57 M FAI, and 0.43 M MACl were dissolved in 1 mL DMF and DMSO (8:1, volume/volume). All stirring processes are carried out in an N_2-filled glovebox. Considering the low dissolution rate at lower temperatures and the high aging rate at higher temperatures of precursor solutions, the stirring time during the preparation process of the precursor solution is different to ensure the corresponding devices have the best performance. for the low-temperature method, the precursor solution was stirred at -20°C for 24 h. For the room-temperature method, the precursor solution was stirred at 20°C for 2 h. For the high-temperature method, the precursor solution was stirred at 60°C for 30 min.

Device Fabrication

FTO-coated glass substrates (Advanced Election Technology Co., Ltd, China, 7 ohm sq^{-1}) were cleaned stepwise with detergent, acetone, isopropanol, and ethanol under sonication for 15 min each. After drying under an N_2 stream, the substrates were treated with ultraviolet ozone for 15 min to generate the hydrophilic surface.

SnO_2 colloid precursor was first diluted to 2.5 wt.% with deionized water. Then, the diluted colloid solution was spin-coated onto FTO substrates at 4000 rpm for 30 s, followed by annealing at 150℃ for 30 min in ambient air. For the low-temperature method, the -20°C precursor solution was spin-coated on the FTO/SnO_2 substrates which have been cooled to -20°C by a semiconductor cooler. Then the film spun at 1000 rpm for 10 s and 5000 rpm for 30 s, when the speed was 5000 rpm for 10 s, 600 μL diethyl ether at -20°C was dripped onto the film. After spin-coating the film annealed at 150℃ for 15 minutes. The ambient temperature during spin coating was controlled at -10℃ to prevent the temperature of the Solution, Anti-solvent, and Substrate from rising quickly, simultaneously higher than other temperatures to ensure that the volatilization of the anti-solvent is not significantly affected. For the room-temperature method, the temperature of precursor solution, FTO/SnO_2 substrates, diethyl ether, and ambient temperature are all set in 20℃. For the high-temperature method, the precursor solution was heated to 60℃, FTO/SnO_2 substrates, diethyl ether, and ambient temperature are all set in 20℃. After cooling to room temperature, the 5 mg/mL of n-Octylammonium iodide dissolved in IPA was spin-coated on top of the perovskite film at 4000 rpm for 30 s. Afterward, 72.3 mg spiro-OMeTAD in 1 mL chlorobenzene with 35 μL Li-TFSI stock solution (260 mg Li-TFSI in 1 mL ACN), 30 μL tBP was deposited on perovskite films at 2500 rpm for 40 s. Finally, the semi-finished devices were transferred into a vacuum chamber for the deposition of MoO_3 (5 nm) and Au (100 nm) electrodes under a base pressure of 4.0×10^{-4} Pa.

Device Measurement

The photovoltaic device performances were measured by using a 2400 Series Source Meter (Keithley Instruments) under an SS-F5-3A solar simulator (AM 1.5G, 100 mW cm^{-2}) (Enlitech) calibrated by an NREL standard Si cell, no additional UV filter equipment was used and mismatch factor was set as 1. The measurements were carried out with the devices inside the glove box (<0.1 ppm O_2 and H_2O). To ensure the accuracy of the JSC measured from J-V scans, a mask with an aperture area of 0.05 cm^2 was covered during the measurement. The J-V curves were

scanned by reverse (forward bias (1.2 V) → short circuit (-0.2 V)) or forward (short circuit (-0.2 V) → forward bias (1.2 V)) scan with a scan rate of 10 mV s^{-1}, and 1 ms delay time. Jsc and Voc dependence on light intensity is measured by the light intensity range from 0 to 100 mW cm^{-2}.

Characterization

The in situ grazing-incidence wide-angle X-ray scattering (GIWAXS) was performed at the BL14BL beamline of the Shanghai Synchrotron Radiation Facility (SSRF) using X-ray with a wavelength of 1.2398 Å. A sealed box with Kapton windows for incoming X-ray and diffracted X-ray, which can be continuously heated and filled with N_2 for sample annealing and observation, several semiconductor plane coolers are placed in the sealed box to create low temperature. Two-dimensional X-ray diffraction (XRD) pattern was obtained by MarCCD at an exposure time of 2 s at a distance of about 327 mm from the sample. The XRD pattern was analyzed using FIT2D software and displayed in the scattering vector q coordinates. X-ray absorption near edge structure (XANES) spectra were measured at room temperature on the 1W1B beamline at the Beijing Synchrotron Radiation Facility (BSRF). Dynamic light scattering (DLS) measurements were performed by ZetaPALS. The measurement was done with a quartz cuvette using multi-size distribution (MSD) mode. Absorption spectra were acquired by SHIMADZU-UV-1750. Steady-state photoluminescence (PL) spectra were recorded on a Hitachi F-4600 fluorescence spectrophotometer. Scanning electron microscopy (SEM) analysis was performed on a Hitachi S-4800 electron microscope. Surface topographies were imaged using an atomic force microscope (AFM)(XE-70). The time-correlated single photon counting (TCSPC) system is adopted (excited by 520 nm laser).

Molecular Dynamics Simulation

Molecular Dynamics (MD) simulations are further employed to study the thermodynamic and structural properties of the PbI_2/FAI/MACL/DMSO/DMF precursor solution at different temperatures. Herein, we construct the coarse-grained model based on our previous simulation study [33-39] and the MARTINI force

field [8]. Note that this simplified model can effectively capture the physicochemical properties of ionic, apolar, and polar species and the simulation can be performed on the relatively larger length and time scales.

In the simulation, we model the Pb^{2+} ions, I^- ions, FA^+ ions, MA^+ ions, Cl^- ions, DMSO molecules and DMF molecules as independent spherical beads (Supplementary Fig. 6), of which the diameters are set as 2.0 Å, 4.12 Å, 5.4 Å, 5.6 Å and 3.6 Å, 4.2 and 4.95 Å, respectively. Each Pb^{2+} carries the positive charge +2*e* at the center, and each monovalent I^-, FA^+, MA^+ or Cl^- ion takes a positive charge +1*e* or a negative charge -1*e* at its center. We classify these beads as charged, apolar and polar ones [40] and model the van der Waals interactions between different species using the truncated and shifted Lennard-Jones (LJ) potential,

$$U_{LJ}(r) = \begin{cases} 4\varepsilon_{\mathrm{LJ}}\left[\left(\frac{\sigma}{r}\right)^{12} - \left(\frac{\sigma}{r}\right)^{6} + S\right], r \le r_c \\ 0, r > r_c \end{cases} \quad \text{S (1)}$$

where the energetic parameter is set as $\varepsilon_{\mathrm{LJ}}$ = 1.0 ~1.5 (which corresponds to 1.0 $k_{\mathrm{B}}T$ ~ 1.5 $k_{\mathrm{B}}T$ at room temperature, T = 298 K) and the cutoff is adjusted in the scope of $r_{\mathrm{c}} = 2^{1/6} \sim 2.0\sigma$ to account for the pairwise interactions between the beforementioned charged, apolar and polar beads [40]. The size parameter between different beads (*i* and *j*) is estimated as $\sigma = (\sigma_{\mathrm{i}} + \sigma_{\mathrm{j}})/2$. We shift the LJ potential to 0 at r_c by the factor *S.* Further, we account for the electrostatic interactions between the ionic beads using Coulomb potential,

$$U_{\mathrm{Coul}} = \frac{Z_i Z_j e^2}{4\pi\varepsilon_0\varepsilon_r r} \quad \text{S (2)}$$

where Z_1 and Z_2 indicate the valences of the charged bead *i* and *j* with a separation distance of *r*, *e* represents the elementary charge, ε_0 is the vacuum permittivity, and the relative permittivity of the precursor solution is set as ε_r = 40, which is in accord to the DMF and DMSO mixture. The U_{Coul} is calculated through the PPPM (particle-particle-particle-mesh) algorithm with an accuracy of 10^{-5}.

The simulations are performed in the canonical (NVT) ensemble with the 3D

periodic boundary conditions using the Large-scale Atomic/Molecular Massively Parallel Simulator (LAMMPS) package [41]. The integration MD time step is fixed as 0.005, corresponding to 6 fs, and the system temperature is controlled via the Langevin thermostat. We set the size of the cubic simulation box as $L \times L \times L$ = 7.2nm×7.2nm×7.2nm, and generate different species in the box to ensure the molar concentration of PbI_2, FAI, MACl as 1.7 mol/L, 1.57 mol/L and 0.43 mol/L, respectively. The molar ratio between DMF and DMSO solvent molecules is 8:1, which is consistent with the case in our experiments. We first employ an athermal procedure for over 10^6 MD steps (6 ns) to eliminate the artificial effect of the initial structures and use another 2×10^6 MD steps (12 ns) simulation to study the structural transition of the solution, during which the temperature gradually decreases from 720K (447℃) to 192K (-81℃). We perform the order of 10^3 simulations with different initial configurations for data analysis. We analyze the structural and dynamic properties of the solution by calculating the static structure factors, radial distribution functions between different components, diffusion coefficient and numbers of neighboring FA^+/MA^+ ions or solvent molecules (DMF and DMSO) around each I^-, which are defined as FA^+/MA^+ ions or solvent molecules falling within a cutoff of 6 Å from the center of each I^-.

TRPL Method

We use a bi-exponential equation: $Y = A_1\exp(-t/\tau_1) + A_2\exp(-t/\tau_2)$ to get the recombination value as reported[52], where the τ_1 and τ_2 are the fast and slow decay time constants namely. The film formed by CSC has a longer lifetime for non-radiative recombination (3218 ns) compared to RSC (1411 ns) and HSC (889 ns).

SCLC Method

To confirm the reduction of defect concentration in the crystal, we use the space charge limited current (SCLC) method to calculate the trap state density in $FAPbI_3$ film. Both the devices are FTO/SnO_2/$FAPbI_3$/PCBM/Ag structure for SCLC measurement. Trap-filled limit voltage (V_{TFL}) means the voltage when all the traps are filled and it can be determined by the equation: $V_{TFL} = eN_{trap}L^2/2\varepsilon\varepsilon_0$ [51,52], where ε (46.9) is the relative dielectric constant of perovskite[53], ε_0 (8.85×10^{-14} F/cm) is

the vacuum permittivity, L (~600 nm) is the thickness of the perovskite, e (1.6×10^{-19} C) is the electronic charge and N_{trap} is the trap-state density.

TDOS Method

For the C-V measurement, the DC bias was from -2 V to 2 V for the samples. The scanning range of the AC frequency was from 10 Hz to 10 MHz. The TDOS ($N_T(E_\omega)$) was described as $N_T(E_\omega) = -\omega(dC/d\omega)(V_{bi}/qkTW)$, where W is the depletion width and V_{bi} is the build-in potential of devices, derived from the Mott-Schottky analysis of the C-V measurement. T, k, q, ω, and C are temperature angular, Boltzmann's constant, elementary charge, frequency, and specific capacitance, respectively. The demarcation energy is: $E_\omega = kTln(\omega_0/\omega)$, where ω_0 is the attempt-to-escape angular frequency (2×10^{11}/s) [54];

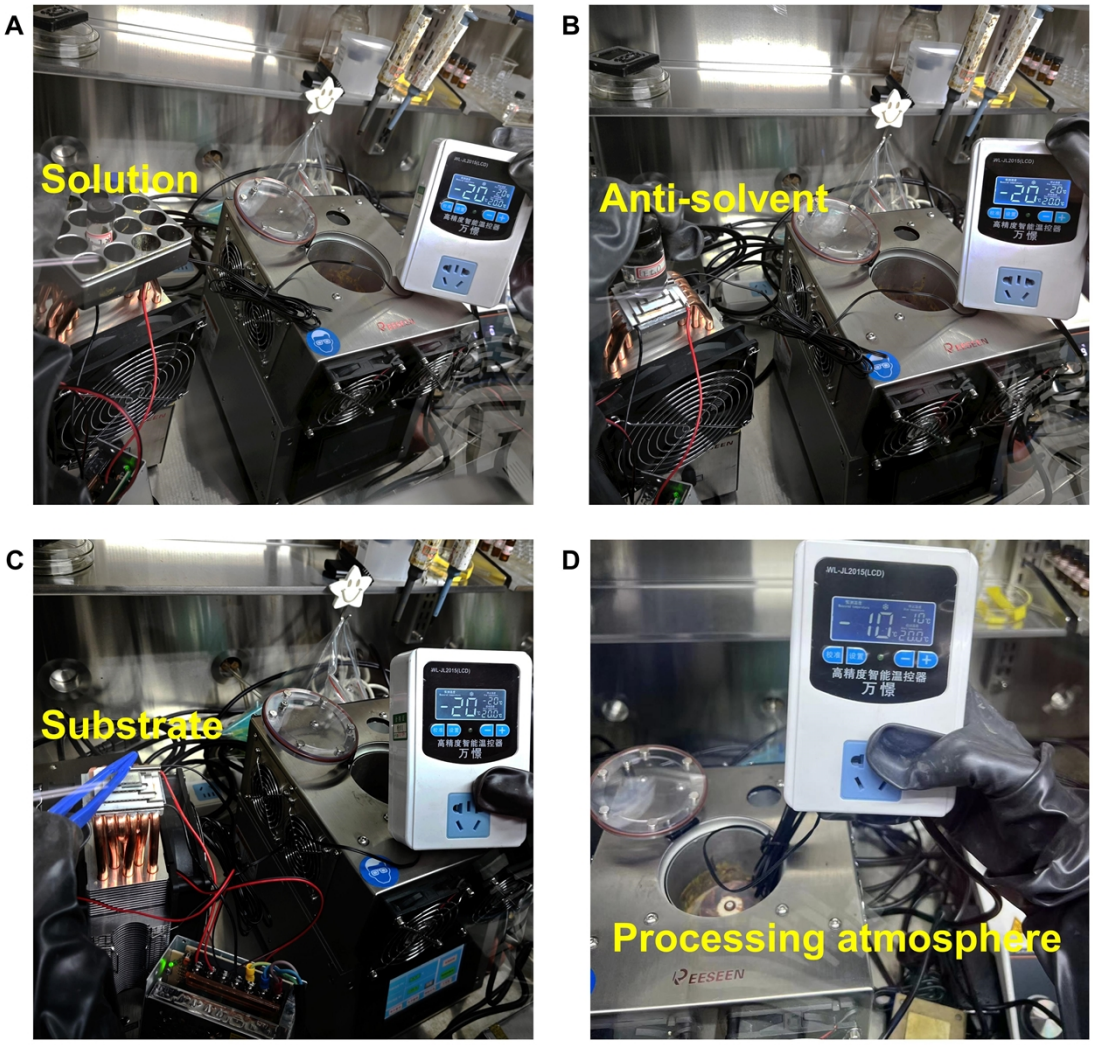

Figure S1. Temperatures corresponding to each part in low-temperature engineering. (A) Solution ~ -20°C, (B) Anti-solvent ~ -20°C, (C) Substrate ~ -20°C and (D) Processing atmosphere ~ -10°C.

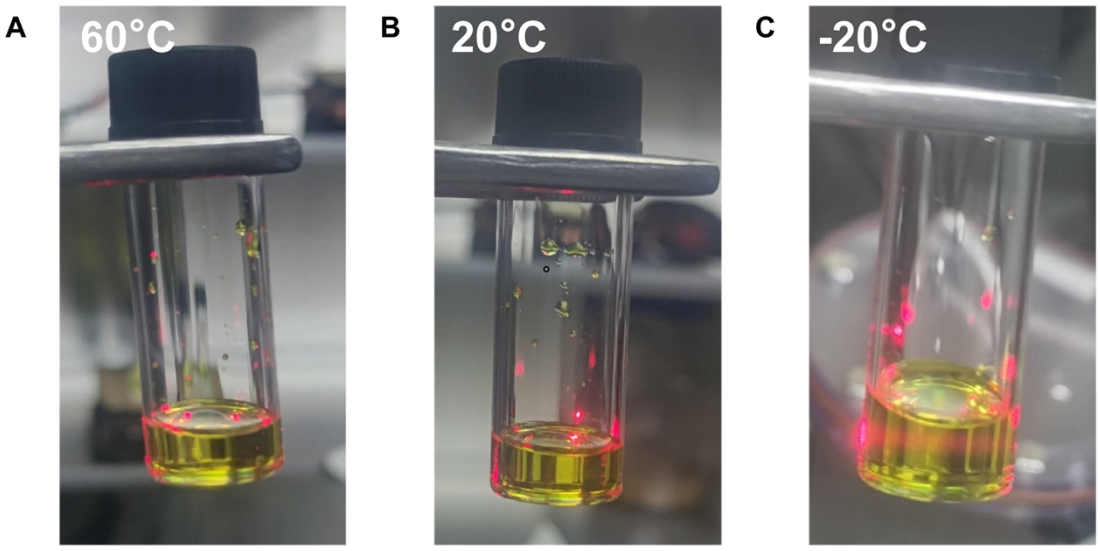

Figure S2. A red laser was shined on $FAPbI_3$ precursor solution in the ratio of 8: 1 (v/v) for DMF: DMSO (1.7 M) to observe the Tyndall effect at temperatures of (A) $T \sim 60°C$, (B) $T \sim 20°C$ and (C) $T \sim -20°C$.

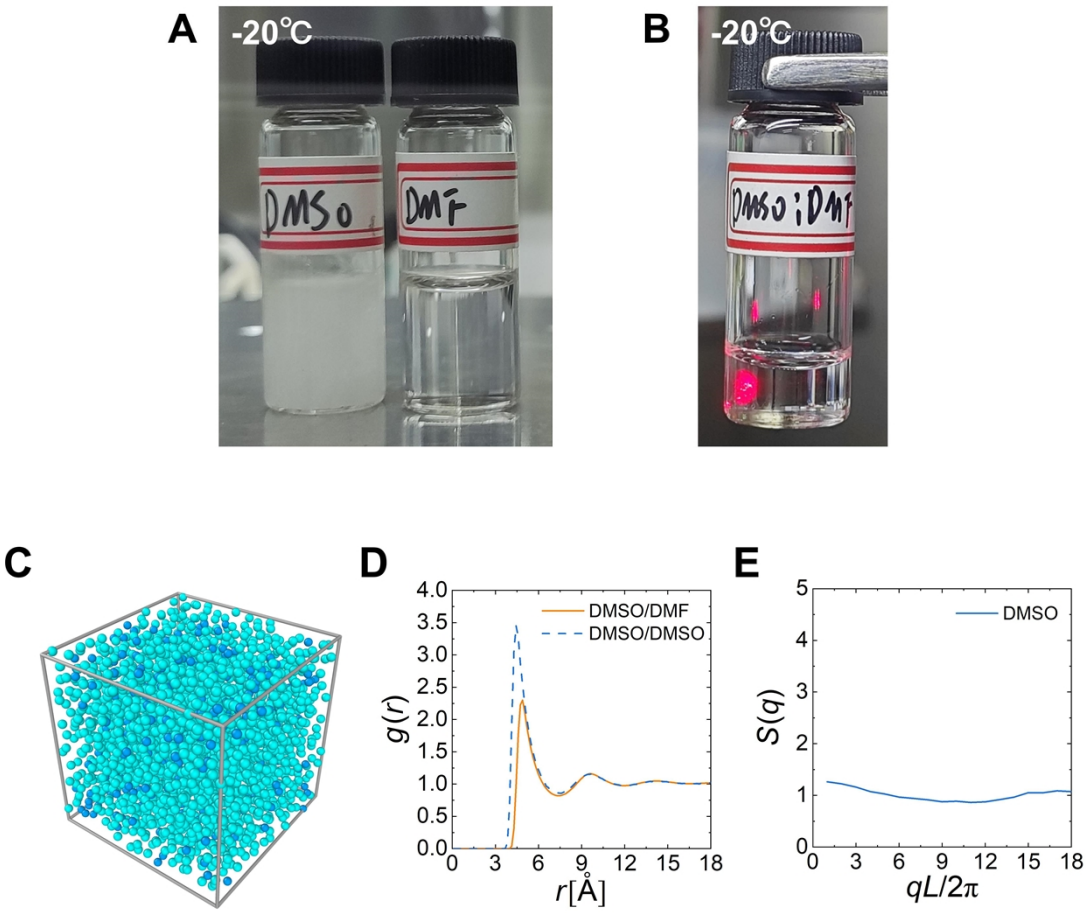

Figure S3. (A) DMF, DMSO, (B) Mixed solution of DMF and DMSO (8: 1) and (C) Perovskite precursor solution when T ~ -20°C (Supplementary Fig. 2C). (C) Typical simulation snapshots for DMF/DMSO (8: 1) solution at temperatures T ~ -20°C (DMSO molecule (dark blue) and DMF molecule (light blue)), (D) Radial distribution functions of DMF/DMSO solution at temperatures T ~ -20°C, (E) Static structural factor for DMSO species at temperatures T ~ -20°C.

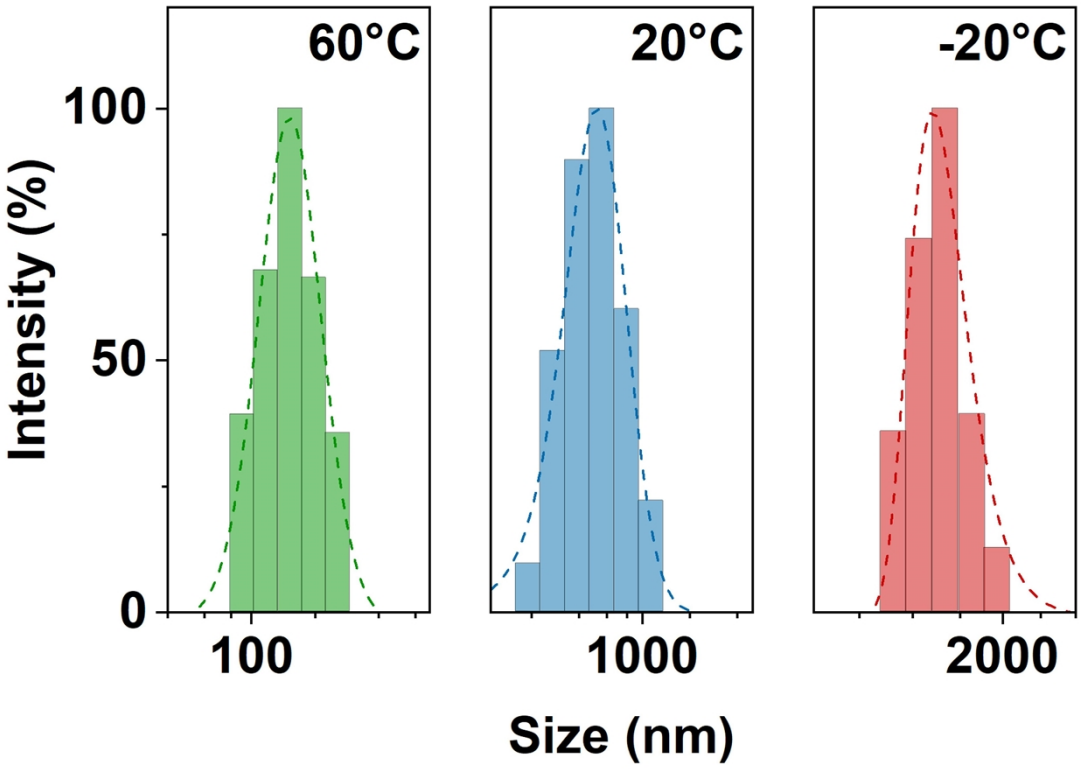

Figure S4. DLS image of $FAPbI_3$ precursor solution in the ratio of 8: 1 (v/v) for DMF: DMSO (1.7 M) at temperatures of $T \sim 60°C$, $T \sim 20°C$, and $T \sim -20°C$.

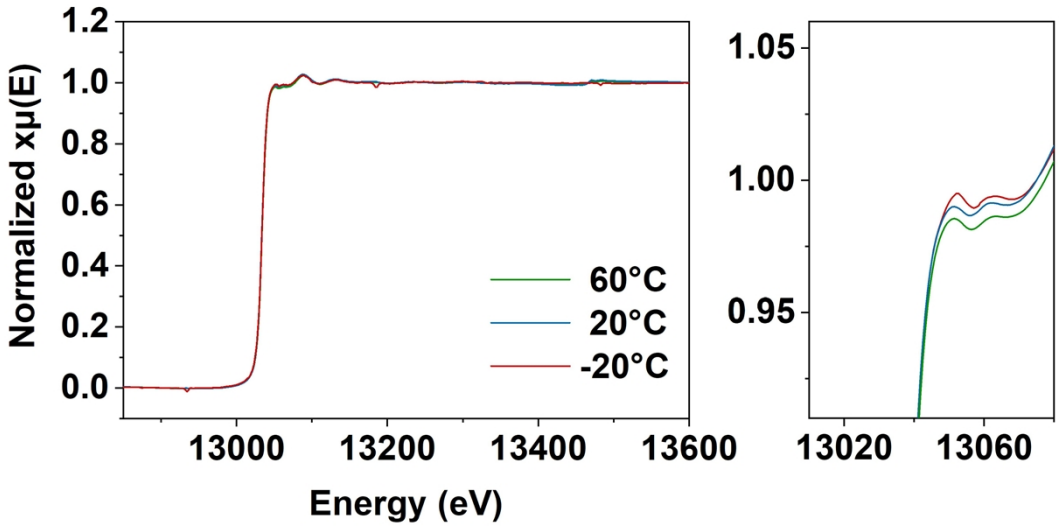

Figure S5. X-ray absorption near edge structure (XANES) spectrum of $FAPbI_3$ precursor solution at temperatures of $T \sim 60°C$, $T \sim 20°C$ and $T \sim -20°C$. Partial enlarged view within the range of 13010 eV to 13080 eV.

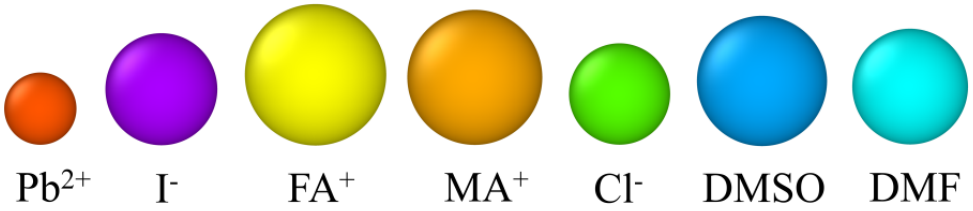

Figure S6. Schematic illustration of coarse-grained Pb^{2+} ion (red), I^- ion (purple), FA^+ ion (yellow), MA^+ ion (orange), Cl^- ion (in green), DMSO molecule (dark blue) and DMF molecule (light blue), respectively.

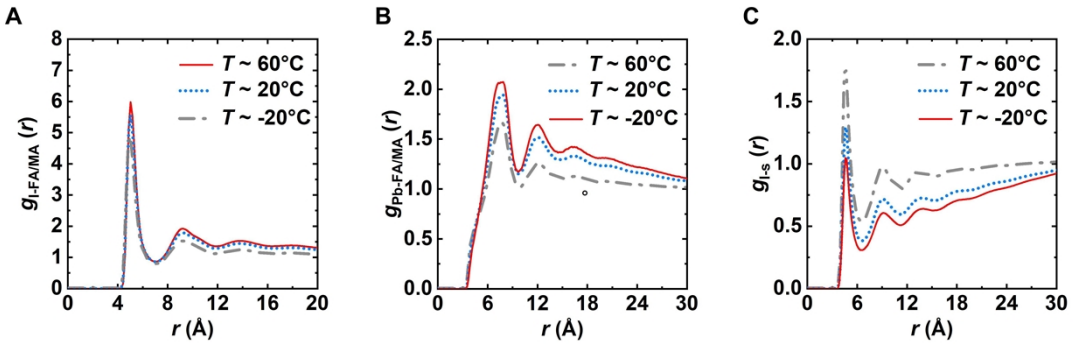

Figure S7. Radial distribution functions of (A) FA^+ and MA^+ ions around each I^- ion ($g_{I\text{-}FA/MA}(r)$), (B) FA^+ and MA^+ ions around each Pb^{2+} ion ($g_{Pb\text{-}FA/MA}(r)$) and (C) solvent (DMF and DMSO) molecules around each I^- ion ($g_{I\text{-}s}(r)$) at different temperatures.

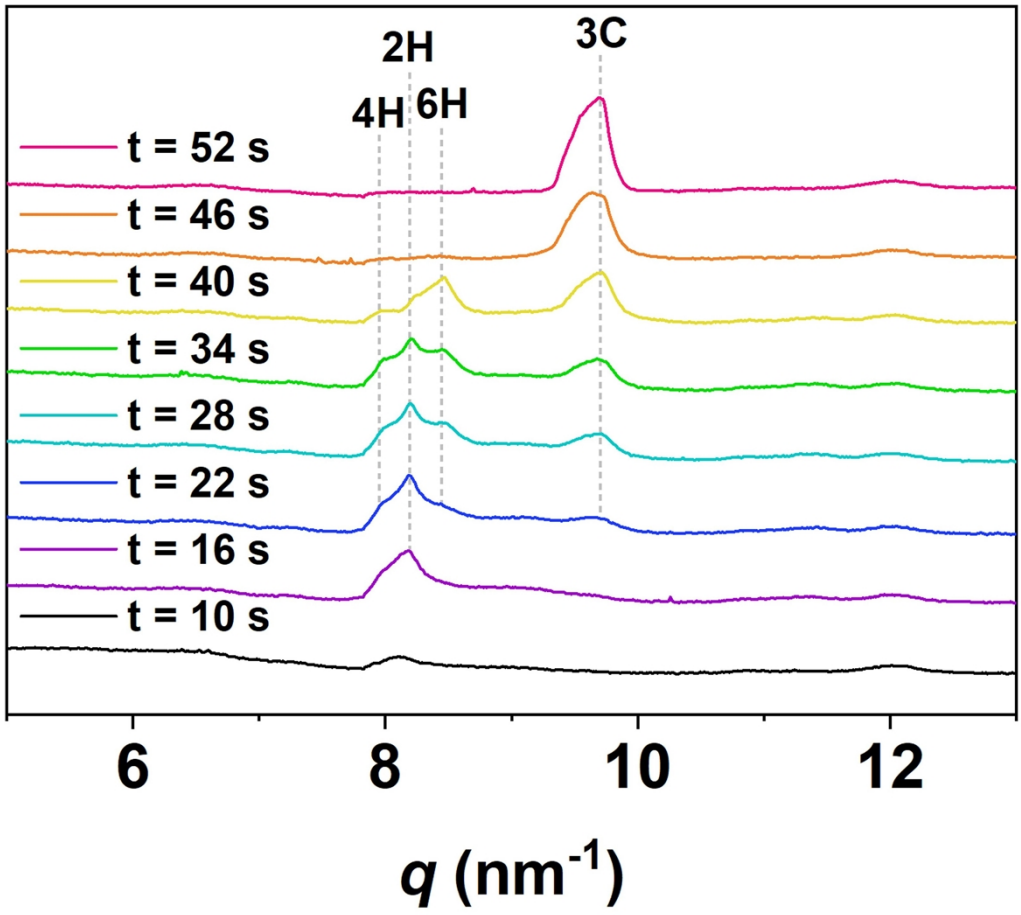

Figure S8. The One-dimensional integral of the two-dimensional diffraction ring with time from Figures 2A (-20°C). During stage II and III, we observed obvious 2H (8.3 nm^{-1}), 4H (8.2 nm^{-1}), 6H (8.6 nm^{-1}), and 3C (9.6 nm^{-1}) peaks.

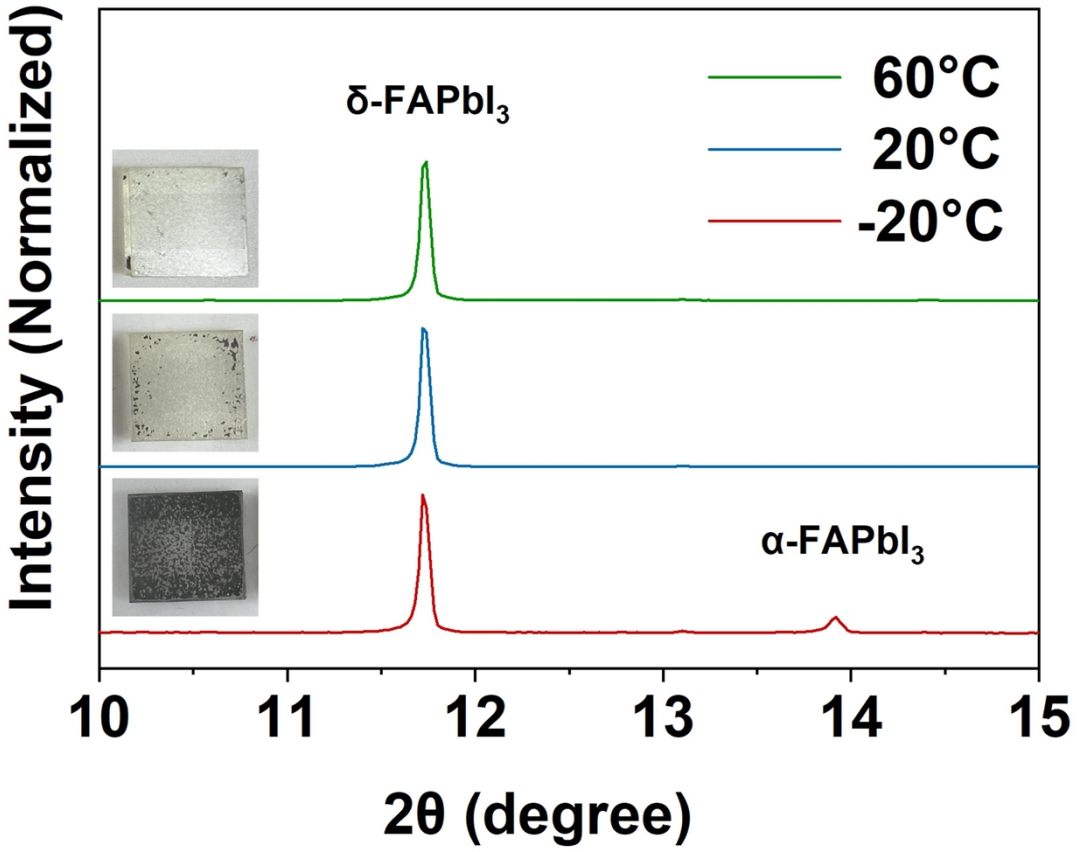

Figure S9. Photos and normalized XRD image of $FAPbI_3$ films formed at temperatures of $T \sim 60°C$, $T \sim 20°C$ and $T \sim -20°C$ without annealing after 30 minutes in an air environment (15°C, 60% humidity). The peak position of 11.7° and 13.9° are attributed to the diffraction peak of δ-$FAPbI_3$ and α-$FAPbI_3$, respectively.

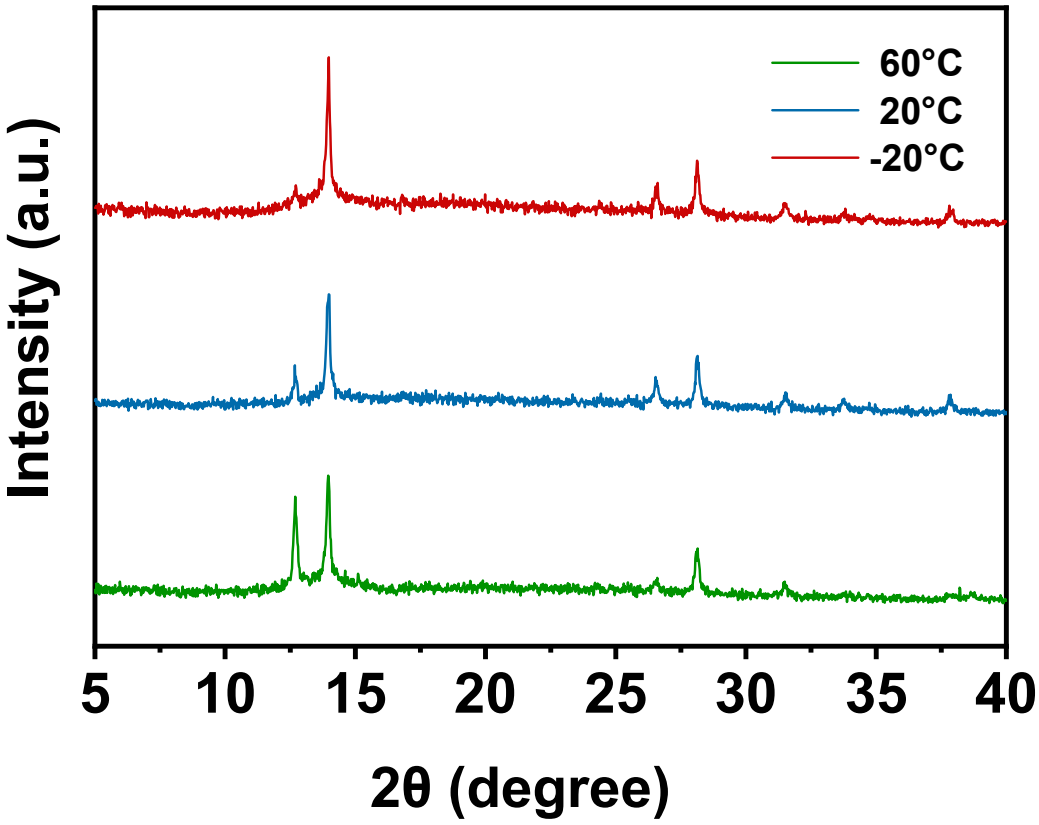

Figure S10. XRD image of $FAPbI_3$ films formed at temperatures of $T \sim 60°C$, $T \sim 20°C$ and $T \sim$ -20°C without MACl.

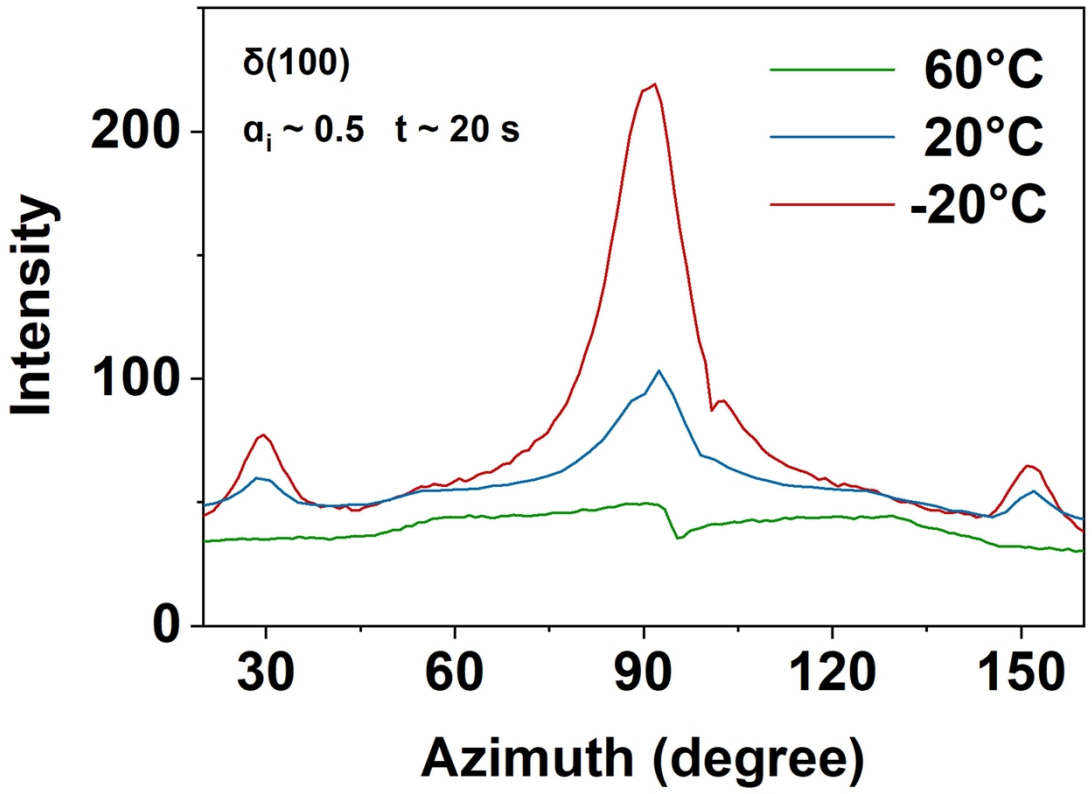

Figure S11. The one-dimensional azimuth integral of the two-dimensional in-situ GIWAXS diffraction pattern of the (100) plane of the δ-$FAPbI_3$ (t = 20 s, α_i = 0.5, exposure for 2 s), corresponding to Fig 3B-D.

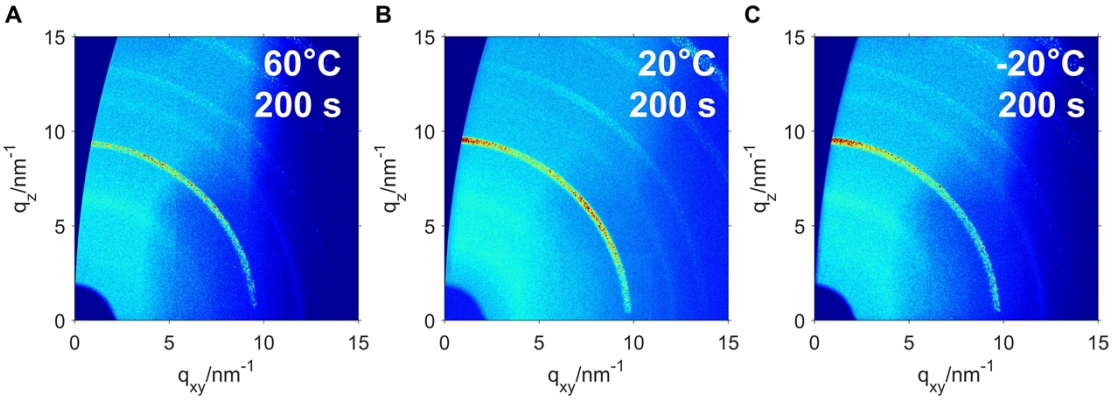

Figure S12. Two-dimensional GIWAXS patterns of the α-$FAPbI_3$ perovskite thin films (t = 200 s, α_i = 0.5, exposure for 2 s). The samples are respectively corresponding to temperatures of (A) T ~ 60°C, (B) T ~ 20°C and (C) T ~ -20°C, intercepted from stage IV of the in-situ GIWAXS characterization (150°C annealing).

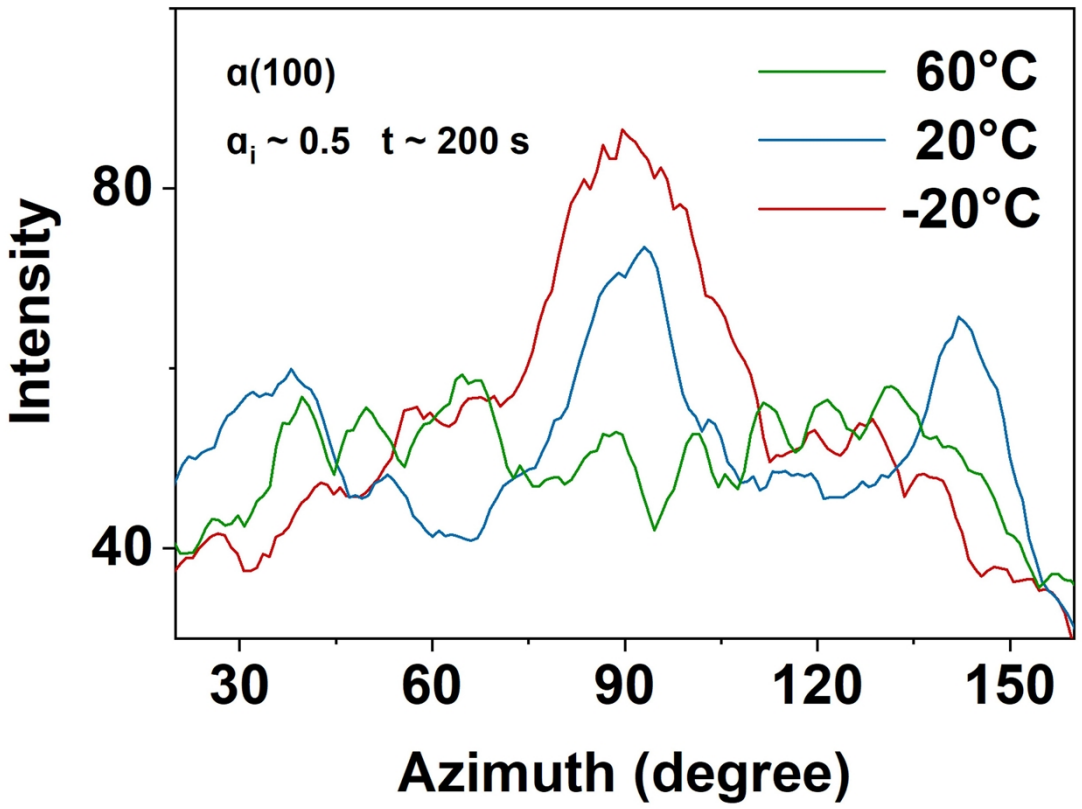

Figure S13. The one-dimensional azimuth integral of the two-dimensional GIWAXS diffraction pattern of the (100) plane of the α-$FAPbI_3$ perovskite thin films (t = 200 s, α_i = 0.5, exposure for 2 s), corresponding to Supplementary Fig. 12.

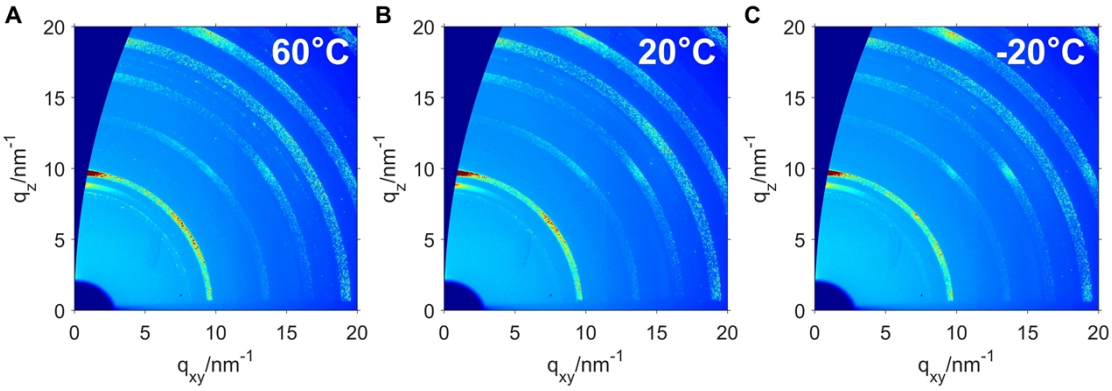

Figure S14. 2D GIWAXS patterns of the prepared α-$FAPbI_3$ perovskite thin films (α_i = 0.5, exposure for 40 s). The samples are formed at temperatures of (A) $T \sim$ 60°C, (B) $T \sim$ 20°C and (C) $T \sim$ -20°C, respectively.

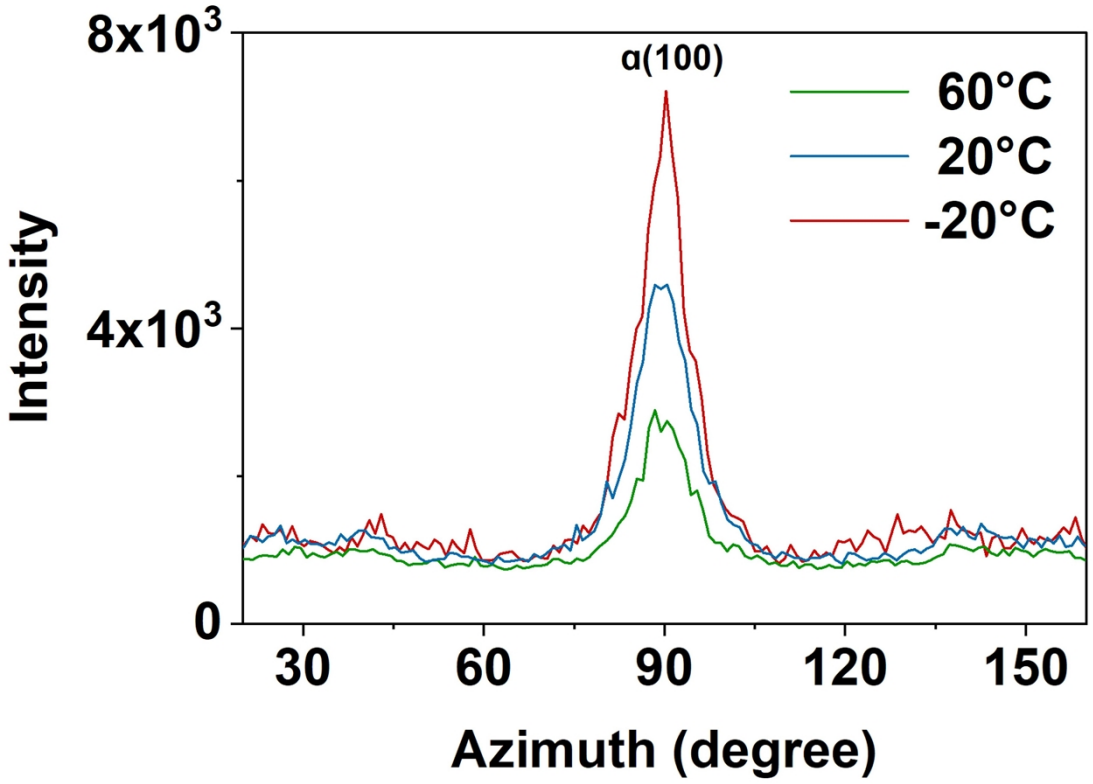

Figure S15. The one-dimensional azimuth integral of the two-dimensional GIWAXS diffraction pattern of the (100) plane of the prepared α-$FAPbI_3$ perovskite thin films (α_i = 0.5, exposure 40 s), corresponding to Supplementary Fig. 14.

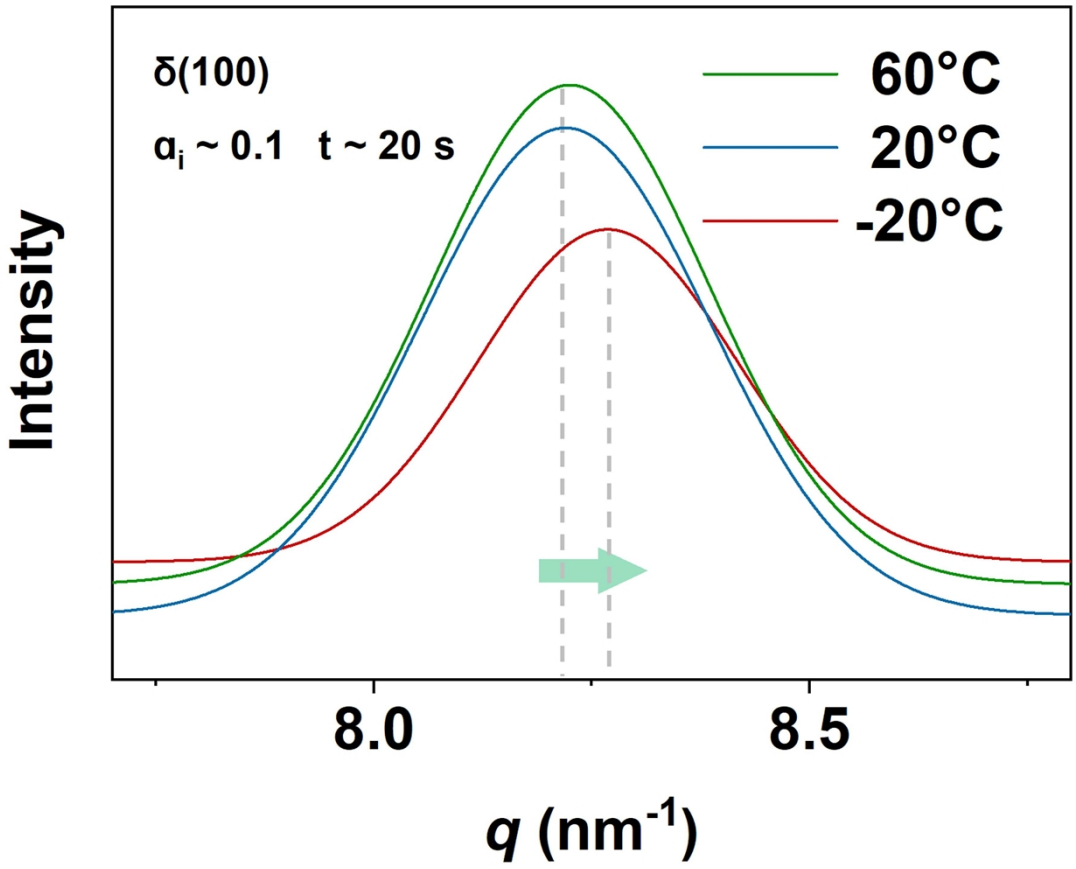

Figure S16. The one-dimensional integral of the two-dimensional in-situ GIWAXS diffraction pattern of the (100) plane of the α-$FAPbI_3$ perovskite thin films (t = 20 s, exposure 10 s, α_i = 0.1). We noticed that the diffraction of the δ-$FAPbI_3$ shifts from 8.22 nm^{-1} (60°C) to 8.27 nm^{-1} (-20°C), consistent with Figure 3E-G, indicating the influence of the intermediate phase on the final α-$FAPbI_3$ perovskite.

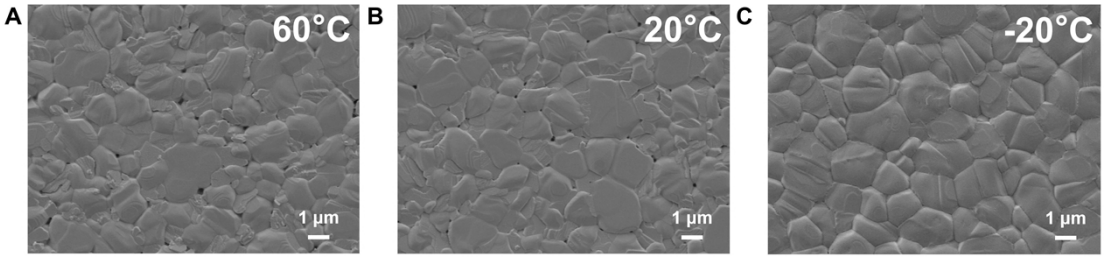

Figure S17. SEM images of $FAPbI_3$ perovskite thin films formed at temperatures of (A) $T \sim 60$°C, (B) $T \sim 20$°C and (C) $T \sim$ -20°C. During the annealing process of $FAPbI_3$ perovskite thin films, the volatilization of DMSO can easily lead to the appearance of pinholes (A, B). When the temperature was decreased to -20°C, the greatly weakened coordination effect between precursor and DMSO reduced the pinholes (C).

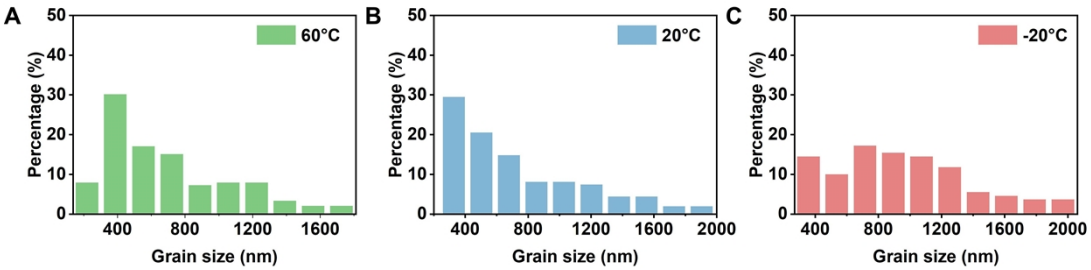

Figure S18. Statistical data of grain size in SEM of $FAPbI_3$ perovskite thin films formed at temperatures of (A) $T \sim 60°C$, (B) $T \sim 20°C$ and (C) $T \sim -20°C$. As shown, the number of small-size grains (<200 nm) at -20°C is significantly reduced compared to 20°C degrees.

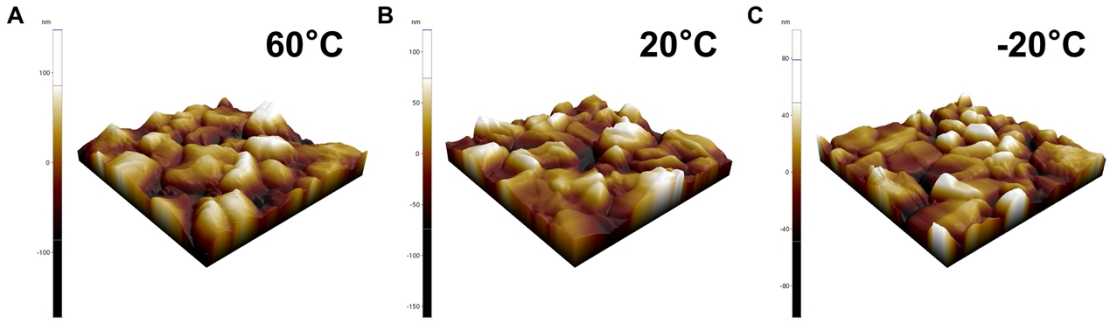

Figure S19. AFM images of $FAPbI_3$ perovskite thin films formed at temperatures (A) $T \sim 60°C$ (R_q = 43.77 nm), (B) $T \sim 20°C$ (R_q = 37.88 nm) and (C) $T \sim -20°C$ (R_q = 24.86 nm).

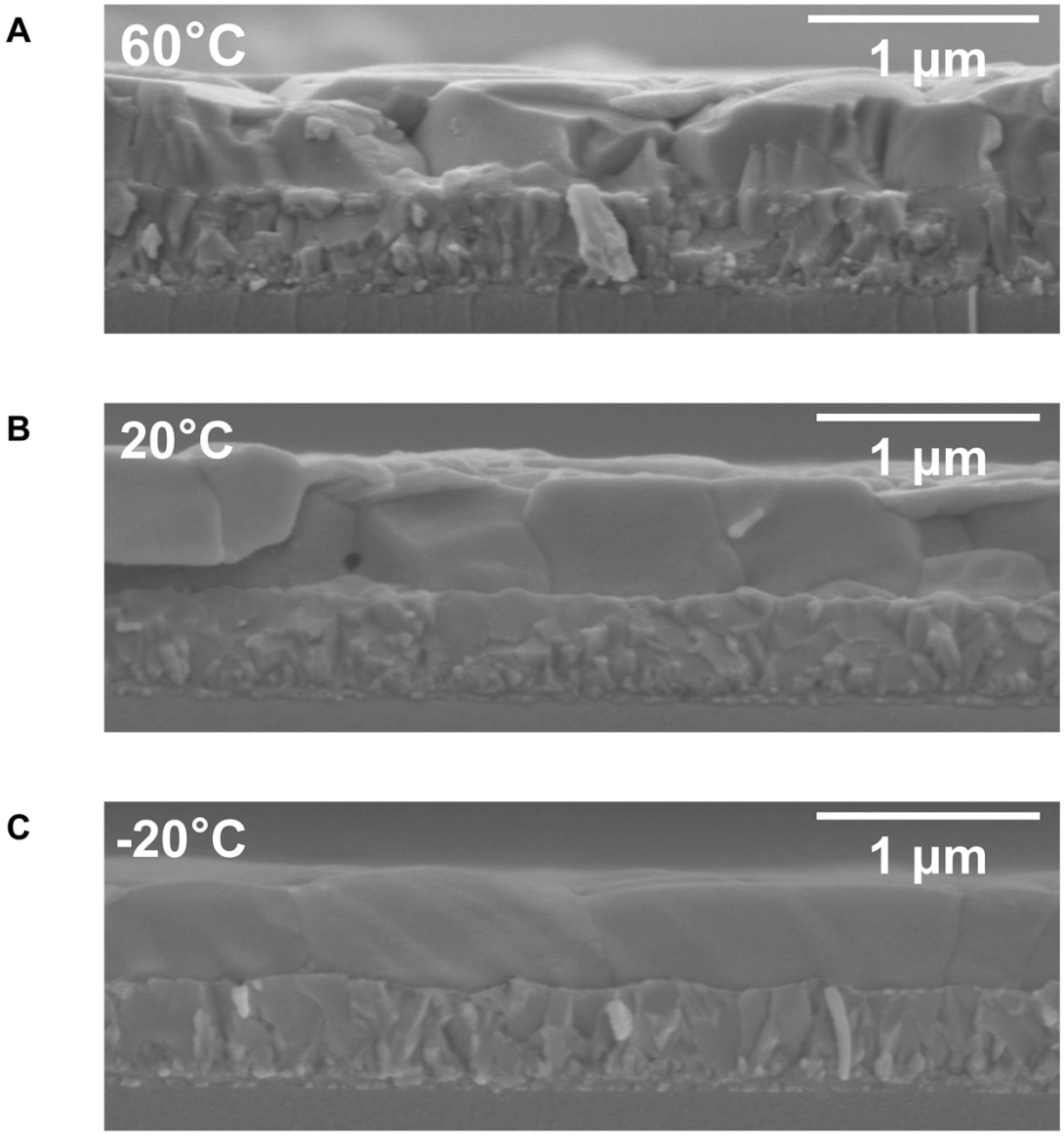

Figure S20. Cross-sectional SEM images of $FAPbI_3$ perovskite thin films formed at temperatures of (A) $T \sim 60°C$, (B) $T \sim 20°C$ and (C) $T \sim -20°C$. In all conditions, the thickness of the films is about 600 nm. The thickness of the films was not affected by temperature-dominated cluster size.

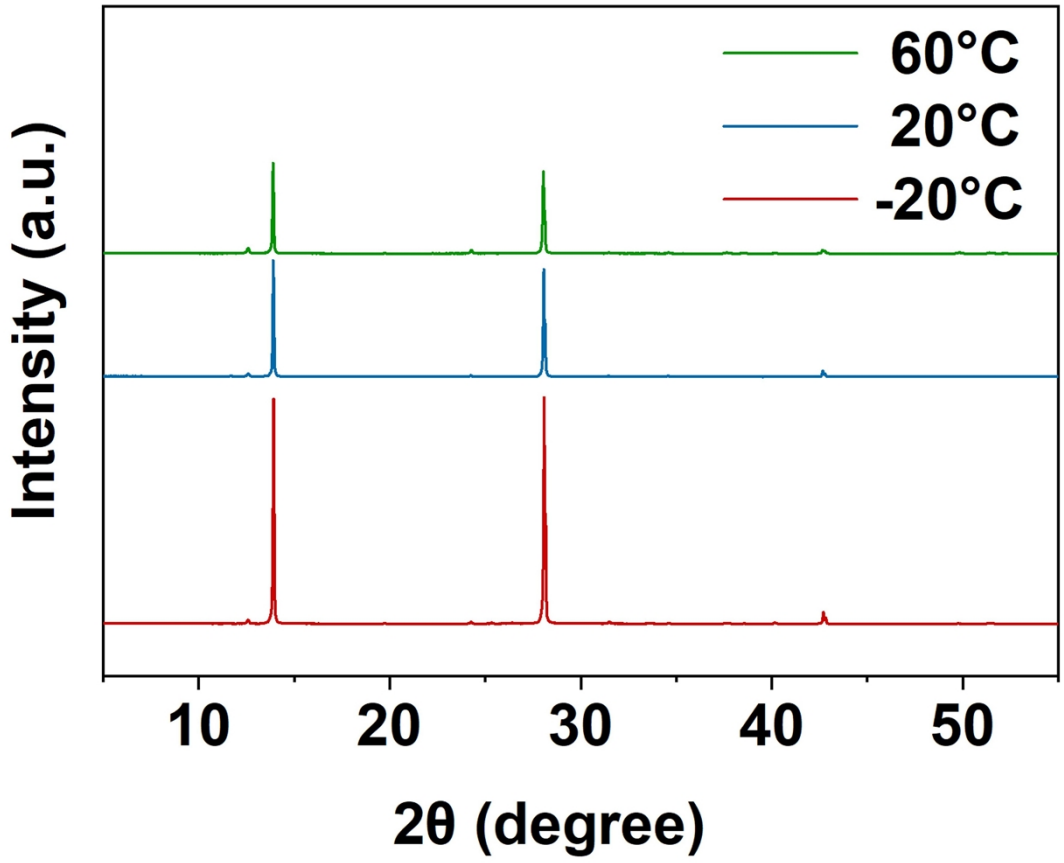

Figure S21. XRD spectra of $FAPbI_3$ perovskite thin films formed at temperatures of $T \sim 60°C$, $T \sim 20°C$ and $T \sim -20°C$.

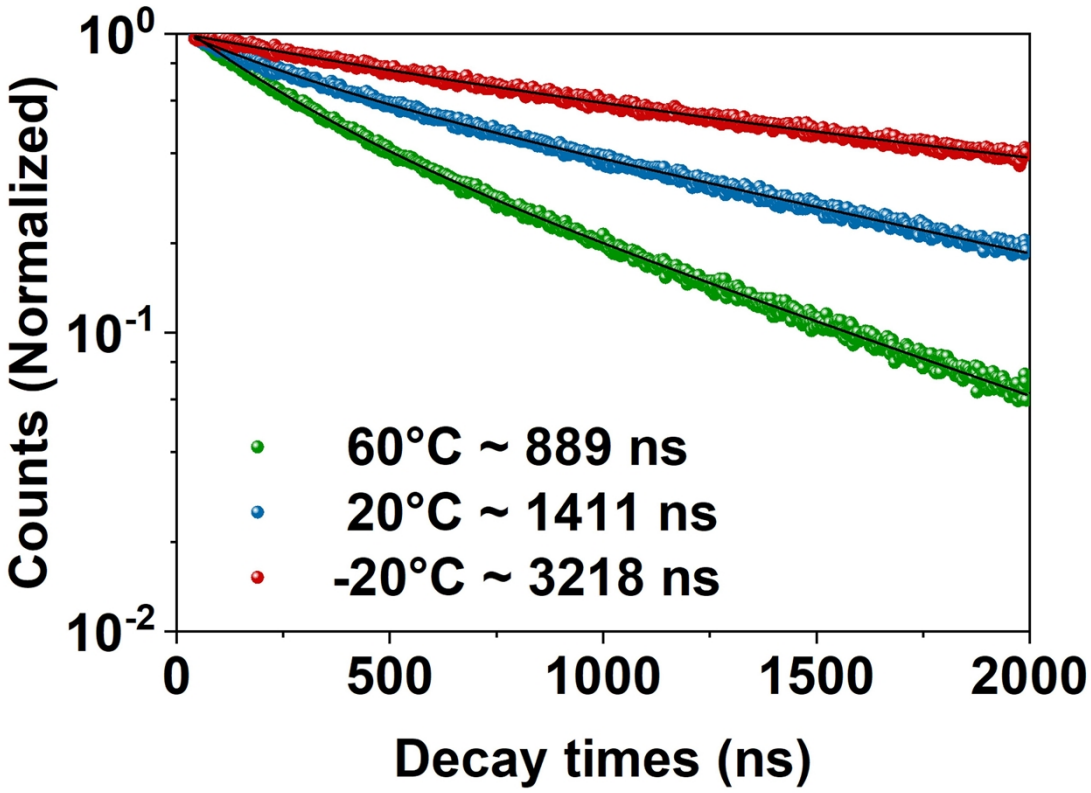

Figure S22. Normalized time-resolved PL decays for $FAPbI_3$ thin films deposited on glass, corresponding to emission wavelength in PL spectra.

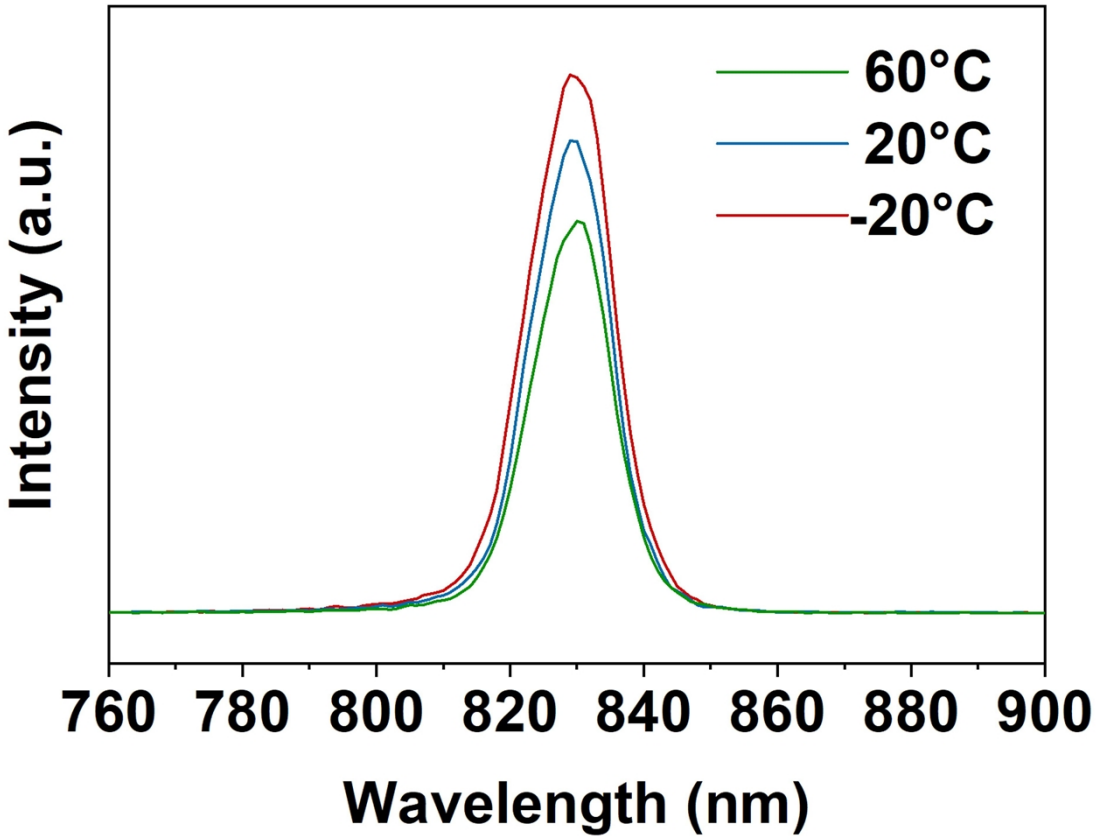

Figure S23. Steady-state PL spectra of $FAPbI_3$ perovskite formed at temperatures of $T \sim 60°C$, $T \sim 20°C$ and $T \sim -20°C$. The PL emission peaks of a-$FAPbI_3$ perovskite thin films under three engineering conditions are all at 830nm, corresponding to a band gap of 1.49eV.

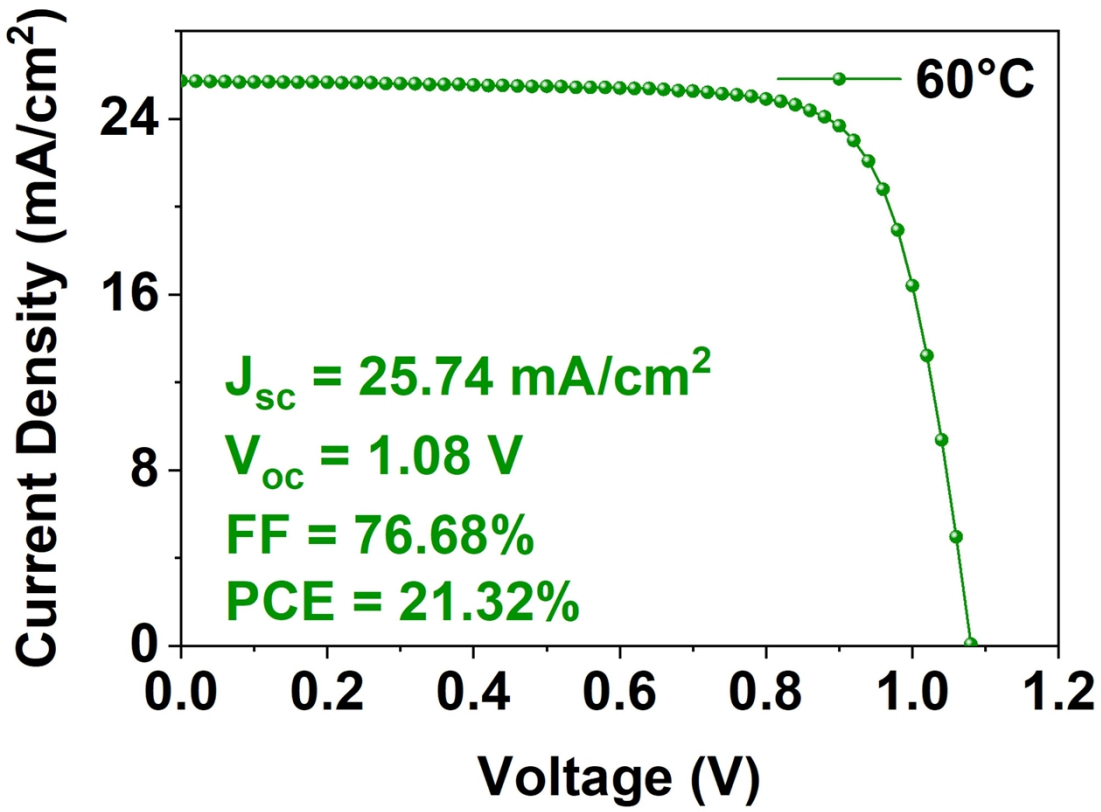

Figure S24. J-V curves of the optimal device with perovskite layer formed at temperatures of $T \sim 60$°C.

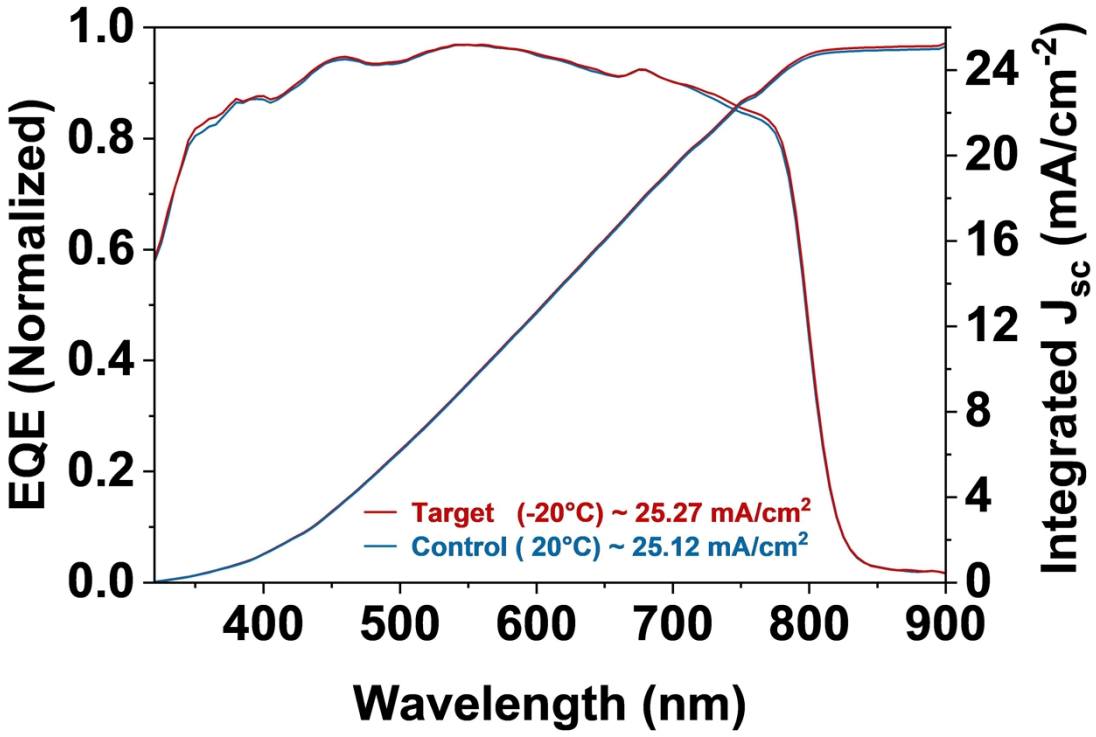

Figure S25. External quantum efficiency (EQE) and integrated J_{SC} for control (20°C) and target (-20°C) devices.

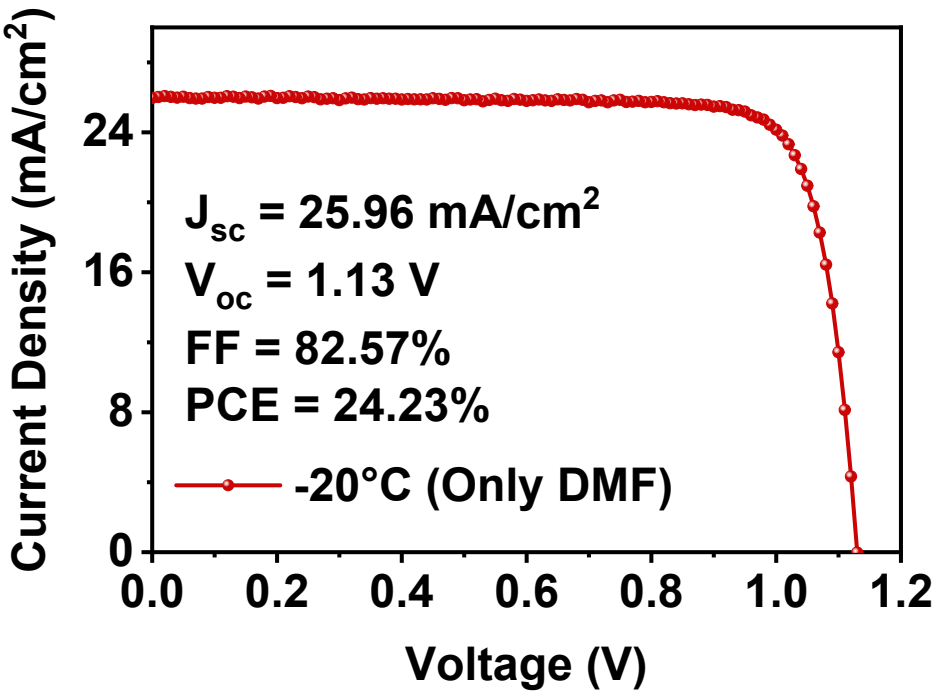

Figure S26. J-V curve of the optimal device by only DMF solution.

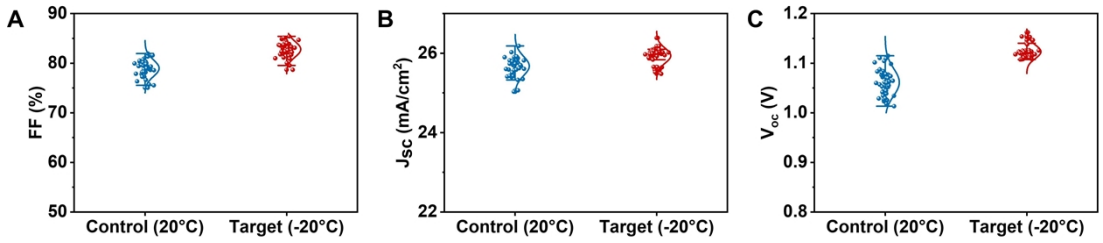

Figure S27. Statistical distribution of (A) FF, (B) J_{sc} and (C) V_{oc} of 40 control and target devices.

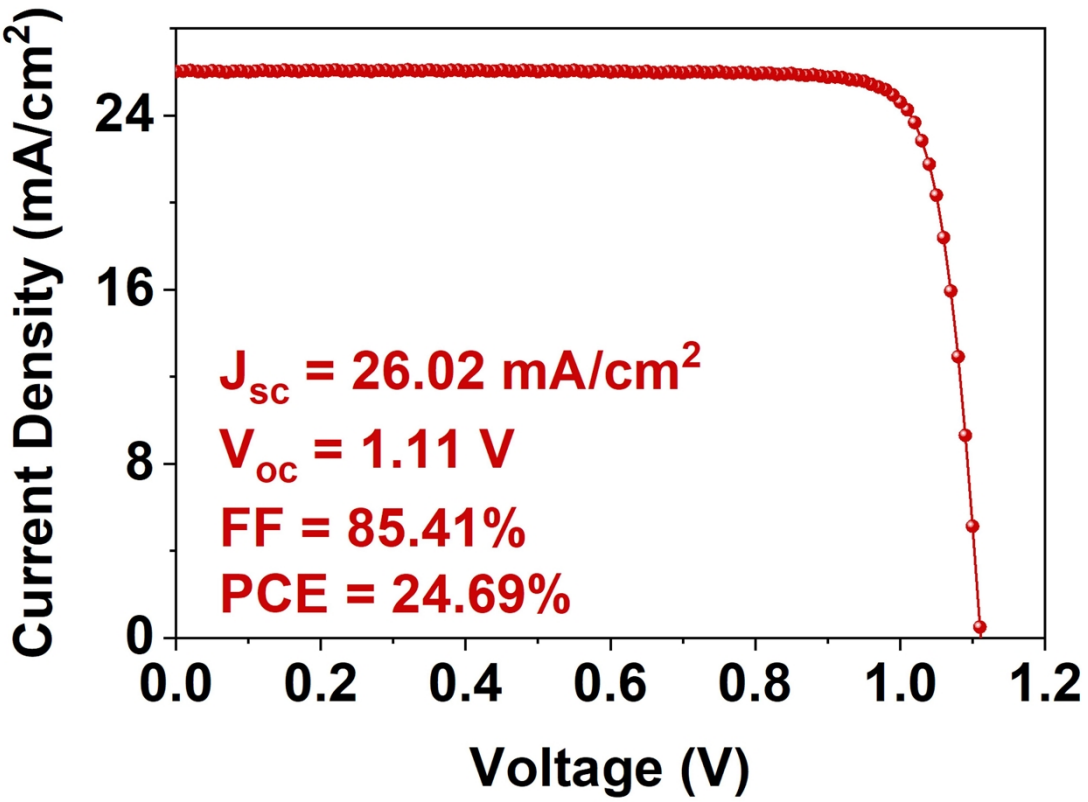

Figure S28. J-V curves of the target device with the highest 85.41% fill factor.

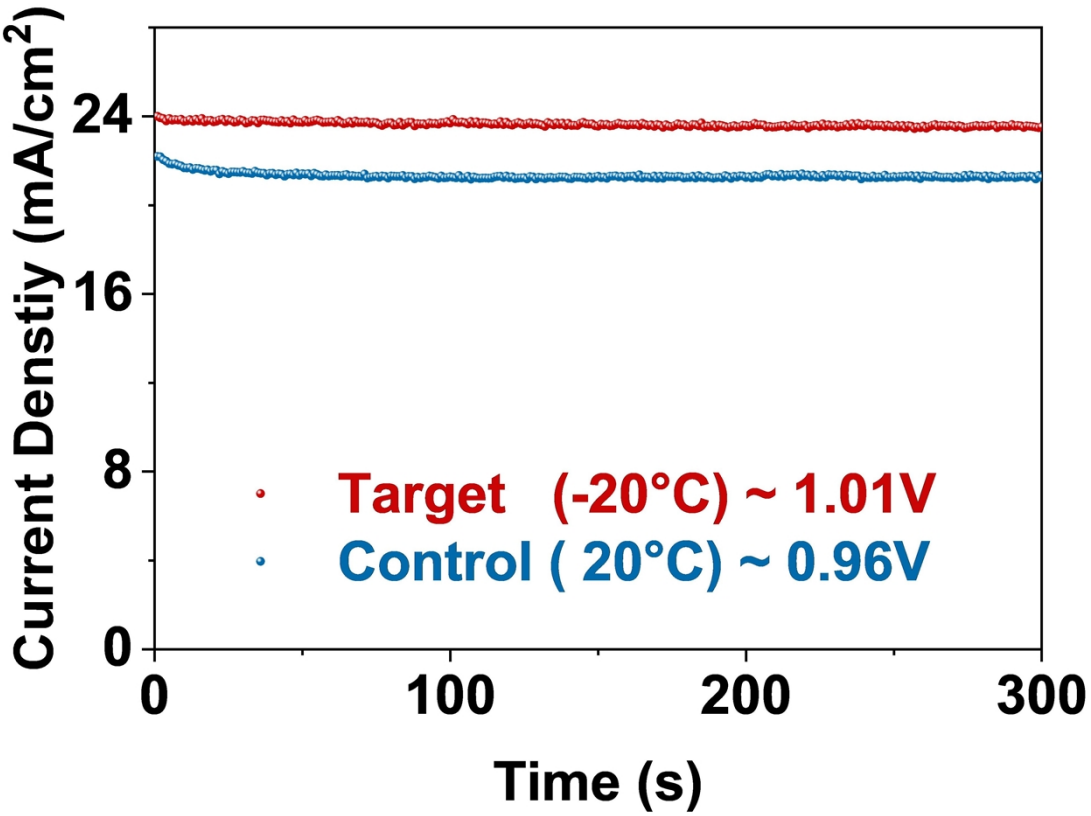

Figure S29. The steady-state output of the control device @0.96 V and target device @1.01 V over 300 s at the maximum power point output. We note that here we chose a control device with a PCE of 24.25% rather than 25.05%, because PCE=24.25% represented the average level of our devices, as shown in the statistical distribution (40 target devices) chart in Figure 4B.

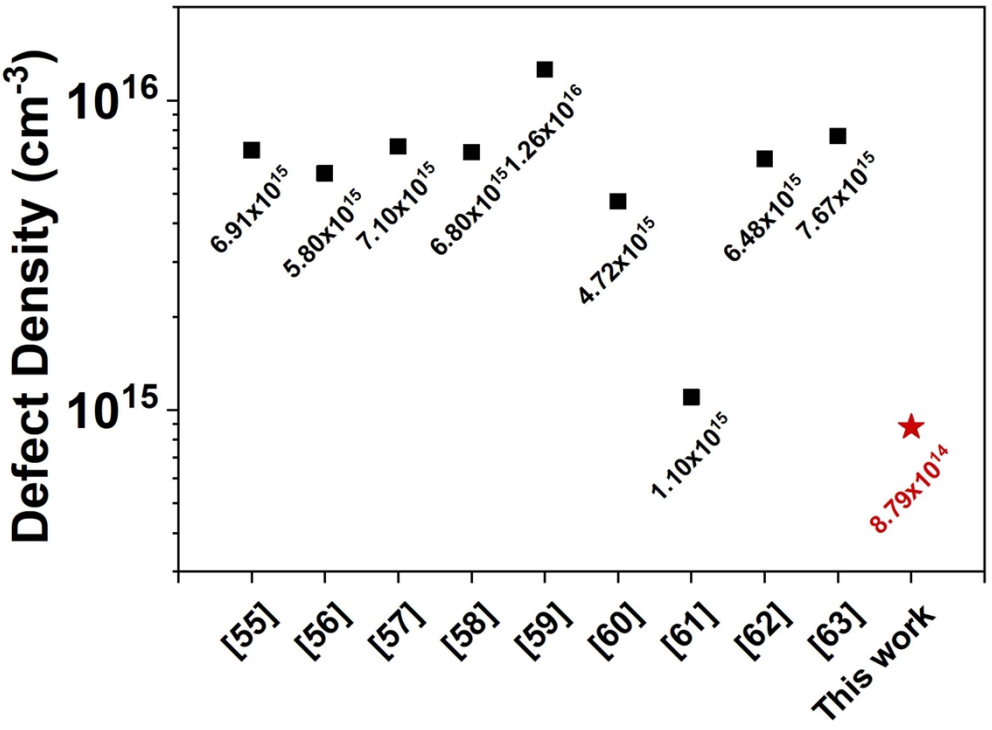

Figure S30. A figure summary of the defect density of best-performing $FAPbI_3$ PSCs by SCLC mothed [55-63].

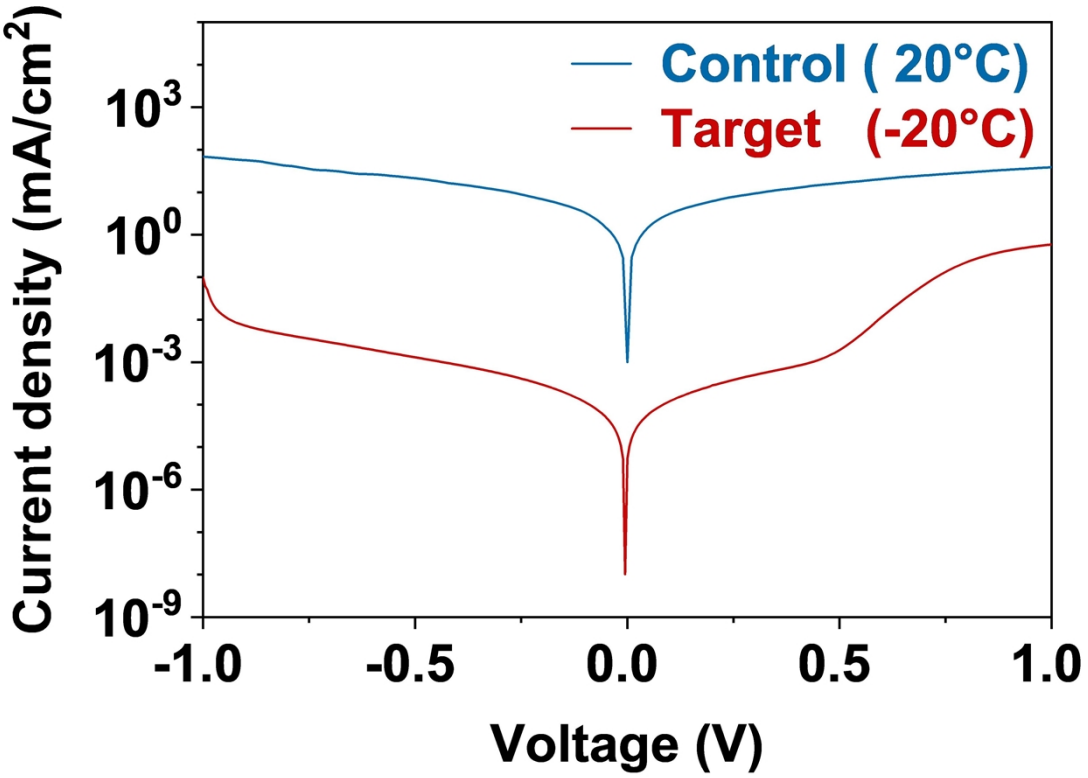

Figure S31. J-V curves of control and target devices under dark condition.

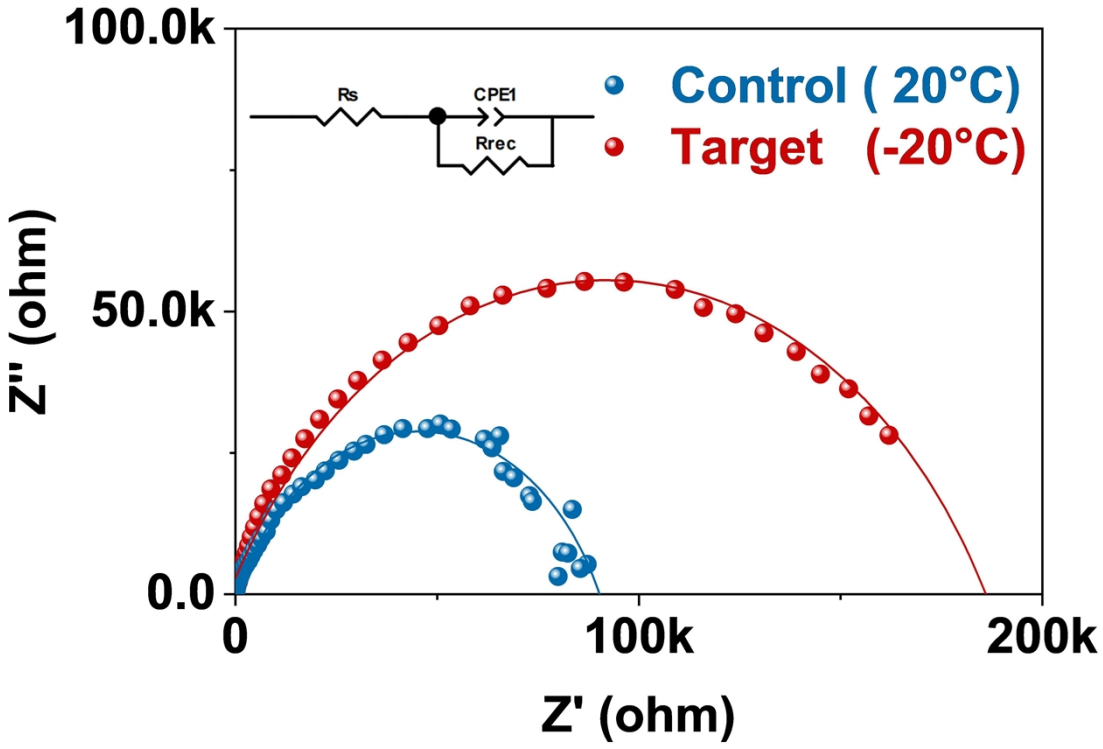

Figure S32. Electrochemical impedance spectroscopy of the PSCs based on the control and target perovskite film.

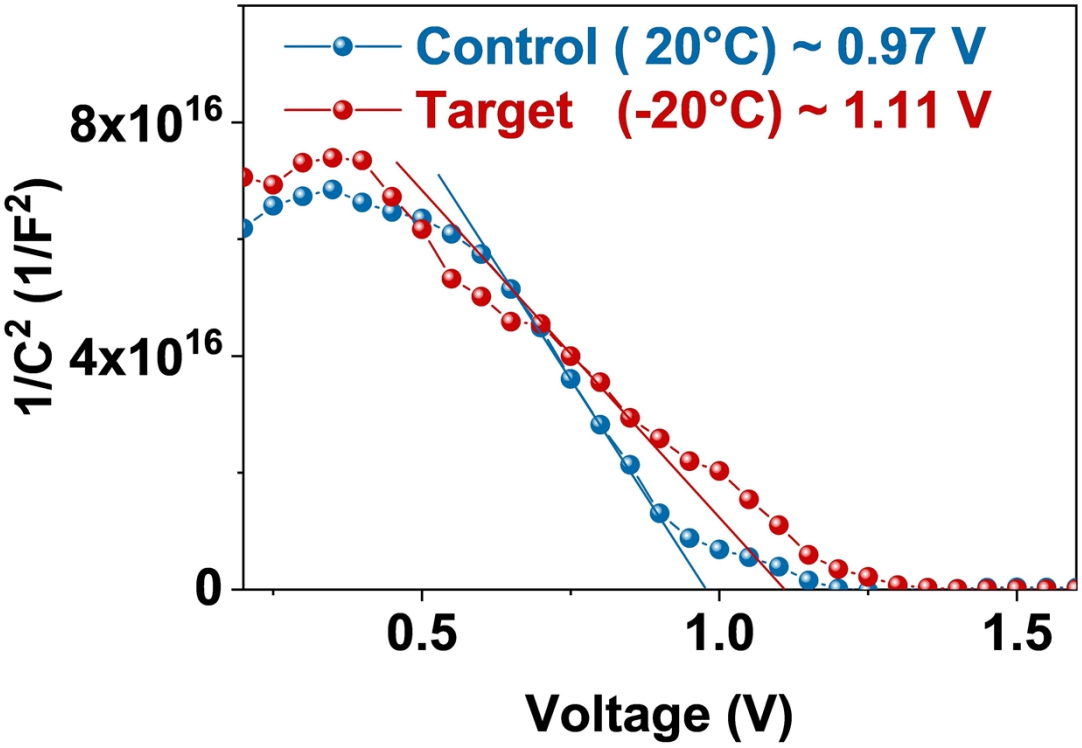

Figure S33. Mott–Schottky plots of control and target devices.

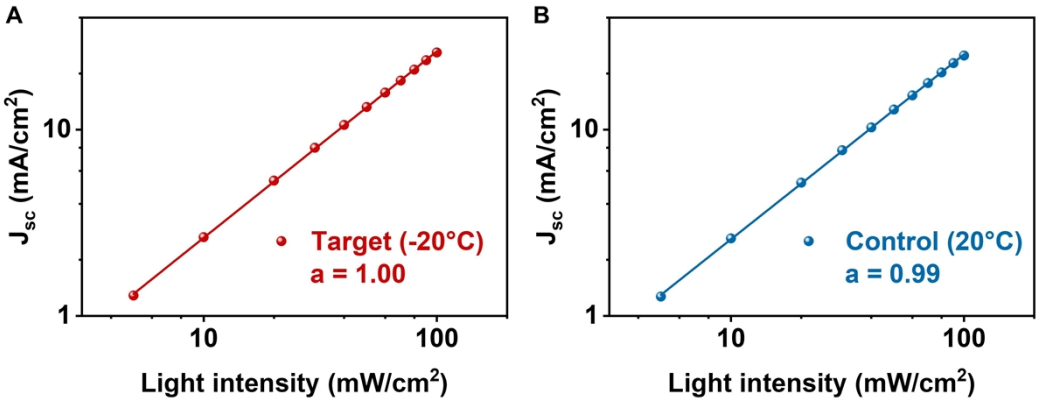

Figure S34. The J_{sc} versus light intensity of PSCs of (A) control and (B) target devices.

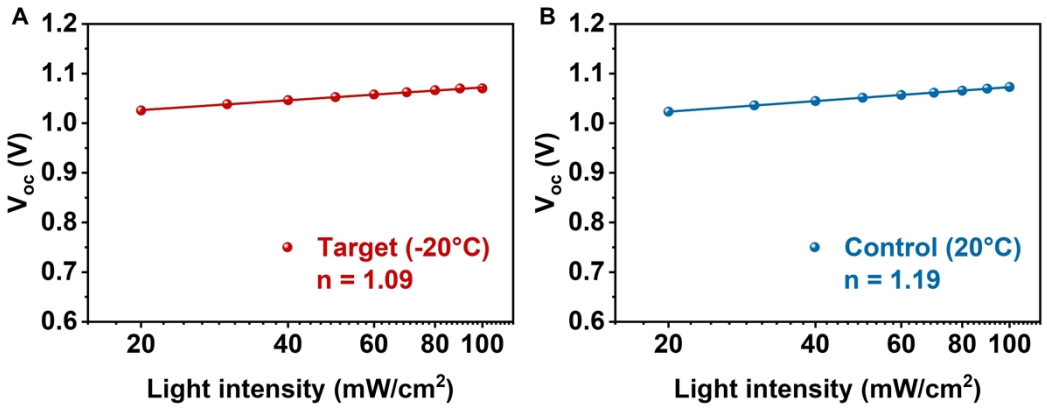

Figure S35. The V_{oc} versus light intensity of PSCs of (A) control and (B) target devices.

Table S1. The $FAPbI_3$ (100) peaks position of the variable angle GIWAXS spectra, the $FAPbI_3$ film formed at -20°C, 20°C, and 60°C respectively.

	α_i = 0.1°	α_i = 0.2°	α_i = 0.3°	α_i = 0.4°	α_i = 0.5°
60°C	9.648	9.659	9.736	9.725	9.725
20°C	9.703	9.725	9.736	9.736	9.736
-20°C	9.758	9.747	9.747	9.736	9.736

Table S2. Performances of the optimal control (20°C) and target (-20°C) devices.

		V_{oc} (V)	J_{sc} (mA/cm^2)	Fill Factor (%)	Efficiency (%)
Target	**Reverse**	1.140	26.01	84.44	25.05
	Forward	1.138	25.99	83.86	24.81
Control	**Reverse**	1.114	25.88	81.33	23.46
	Forward	1.101	25.90	79.94	22.81

Movie S1

Molecular dynamics simulation animation of precursor solutions from 60°C to -20°C.

REFERENCES AND NOTES

50 H. Min, M. Kim, S.-U. Lee, H. Kim, G. Kim, K. Choi, J. H. Lee, S. I. Seok, *Science* **2019**, 366, 749-753.

51. A. Sussman, *J. Appl. Phys.* **1967**, 38, 2738-2748.

52. M. Taukeer Khan, A. Almohammedi, S. Kazim, S. Ahmad, *Chem. Rec.* **2020**, 20, 452-465.

53. Y. Zhang, T. Kong, H. Xie, J. Song, Y. Li, Y. Ai, Y. Han, D. Bi, *ACS Energy Lett.* **2022**, 7, 929-938.

54. M. Samiee, S. Konduri, B. Ganapathy, R. Kottokkaran, H. A. Abbas, A. Kitahara, P. Joshi, L. Zhang, M. Noack, V. Dalal, *Appl. Phys. Lett.* **2014**, 105, 153502.

55. I. S. Yang, N. G. Park, *Adv. Funct. Mater.* **2021**, 31, 2100396.

56. J. W. Lee, S. Tan, T. H. Han, R. Wang, L. Z. Zhang, C. Park, M. Yoon, C. Choi, M. J. Xu, M. E. Liao, S. J. Lee, S. Nuryyeva, C. H. Zhu, K. Huynh, M. S. Goorsky, Y. Huang, X. Q. Pan, Y. Yang, *Nat. Commun.* **2020**, 11, 5514.

57. S. Zhan, Y. W. Duan, Z. K. Liu, L. Yang, K. He, Y. H. Che, W. J. Zhao, Y. Han, S. M. Yang, G. T. Zhao, N. Y. Yuan, J. N. Ding, S. Liu, *Adv. Energy Mater.* **2022**, 12, 2200867.

58. X. Y. Du, J. Zhang, H. Su, X. Guo, Y. J. Hu, D. L. Liu, N. Y. Yuan, J. N. Ding, L. L. Gao, S. Liu, *Adv. Mater.* **2022**, 34, 2204098.

59. X. X. Xu, Y. H. Sun, D. C. He, Z. Liang, G. Z. Liu, S. D. Xu, Z. Q. Li, L. Z. Zhu, X. Pan, *J. Mater. Chem. C* **2021**, 9, 208-213.

60. C. M. Tian, Y. Zhao, X. F. Han, B. Li, Y. C. Rui, H. Xiong, Y. Qiu, W. An, K. R. Li, C. Y. Hou, Y. G. Li, H. Z. Wang, Q. H. Zhang, *Chem*. *Eng*. *J*. **2023**, 452, 137806.

61. G. D. Li, J. Song, J. H. Wu, Y. Xu, C. Y. Deng, Z. Y. Song, X. B. Wang, Y. T. Du, Q. Chen, R. S. Li, W. H. Sun, Z. Lan, *Chem*. *Eng*. *J*. **2022**, 449, 137806.

62. S. Y. Abate, Q. Q. Zhang, Y. F. Qi, J. Nash, K. Gollinger, X. C. Zhu, F. X. Han, N. Pradhan, Q. L. Dai, *ACS Appl. Mater. Interfaces* **2022**, 14, 28044-28059.

63. Z. X. Jiang, J. F. Fu, J. J. Zhang, Q. Y. Chen, Z. L. Zhang, W. X. Ji, A. L. Wang, T. Y. Zhang, Y. Zhou, B. Song, *Chem*. *Eng*. *J*. **2022**, 436, 135269..